A Study of Breakaway Oxidation of 9Cr-1Mo Steel in a Hot CO_2 Atmosphere using Raman Spectroscopy

C. Liu[1,a], P.J. Heard[1,b], S.J. Greenwell[1,c], and P.E.J. Flewitt[1,2,d].

[1]Interface Analysis Centre, HH Wills Physics Laboratory, University of Bristol, Bristol, BS8 1TL, UK
[2]HH Wills Physics Laboratory, University of Bristol, Bristol, BS8 1TL, UK

[a]Chong.Liu@bristol.ac.uk, [b]Peter.Heard@bristol.ac.uk,
[c]S.J.Greenwell@bristol.ac.uk, [d]Peter.Flewitt@bristol.ac.uk.

Abstract. The microstructure of the oxide scale and metal bulk in ferritic 9Cr-1Mo steel was observed in order to explore the oxidation and carburisation mechanisms upon exposure to a CO_2 gas environment at high temperature and high pressure. An experimental 9Cr-1Mo steel sample that had been oxidised at 580ºC for more than 165000 hrs in the coolant gas consisting primarily of CO_2 gas was analysed. In order to elucidate the oxidation characterisation, scanning Raman spectrometry was used to analyse the oxide close to the metal/oxide interface. Carbon was found to be deposited in the spinel layer. The microstructure and the distribution of elemental chemical composition were examined and analysed using optical and high-resolution scanning electron microscopy combined with energy dispersive X-ray analysis. Raman signals from the oxide scale were analysed in order to explore the possibility of deriving strain information close to the oxide-metal interface. The results are discussed with relation to understanding the mechanisms of oxidation and carburisation which aim to underpin extension of the service life of components fabricated from this steel.

Keywords: 9Cr-1Mo steel, Raman spectroscopy, oxidation, carburisation

Introduction

9Cr-1Mo steel is used as a structural material in advanced gas-cooled nuclear reactors (AGR) operated in the UK [1-3]. The selection of this steel was based on its excellent high temperature creep strength, low oxidation rate and ease of weldability[4]. However, changes in the physical, mechanical and chemical properties occur as a result of thermal aging and exposure to the hot CO_2 coolant gas mixture. There is a general consensus that the corrosion in CO_2 gas at high temperature proceeds in two stages corresponding to the following reactions[5]:

$$3M + 4CO_2 \rightarrow M_3O_4 + 4CO \quad (1)$$

$$4CO \rightarrow 2CO_2 + 2C \downarrow \quad (2)$$

where M represents Fe and Cr. Previous workers have proposed that at 550°C a duplex oxide is formed via these reactions by outward growth of magnetite (Fe_3O_4) at the oxide-gas interface and inward growth of spinel ($Fe_xCr_{3-x}O_4$) at the metal/oxide interface[6-8]. In addition carbon diffuses inwards resulting in carburisation of the metal matrix and production of carbide precipitates [9-12]. Equations (1) and (2) represent the processes of oxidation and carburisation respectively. Under certain conditions, oxidation can proceed rapidly, resulting in a thick oxide composed of multi-layered spinel and magnetite[13]. This breakaway oxidation is influenced by sample geometry and commonly occurs at sharp corners or edges. In addition, oxide cracking frequently accompanies breakaway oxidation, but it is unclear whether this is a cause of the breakaway, for example allowing ingress of gas to the metal-oxide interface, or whether it occurs after breakaway initiation due to rapid oxide growth. Figure 1(a) shows a schematic diagram of the oxidation process, while Figure 1(b) shows the stages of oxide growth including breakaway. An understanding of the strain fields within the oxide close to the interface with the metal would be instructive in determining whether cracking is a cause or an effect of breakaway oxidation[14].

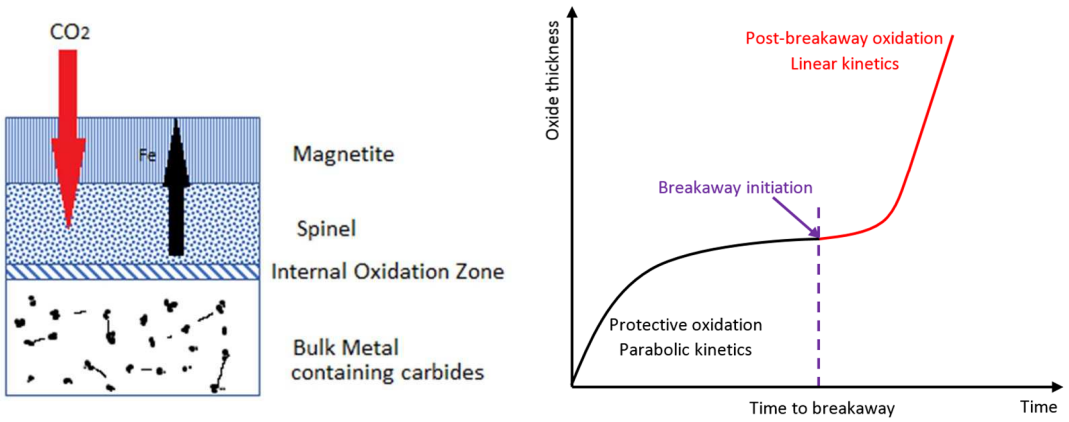

a) b)

Figure 1: a) Schematic of oxidation process. b) Oxide thickness against exposure time for both protective and breakaway oxidation.

Materials and experiments

An experimental sample of ferritic 9Cr-1Mo steel was prepared and the bulk chemical composition from wet analysis provided by EDF Energy is analysed from original cast FA171 which is shown in Table 1. The specimen was exposed in an autoclave, located within an AGR reactor containing flowing gas that is electrically heated. The representative conditions within the autoclave are flowing CO_2 gas containing small amounts of CO, H_2, H_2O and CH_4, at 580 ºC with the sample exposed for about 165000 hrs.

Table 1: Chemical composition of sample before exposure.

Elements	C	Si	S	P	Mg	Cr	Ni	Mo	Cu	Co	Sn
Wt.% min	0.11	0.61	0.007	0.008	0.47	8.98	0.18	0.93	0.14	0.017	0.015
Wt.% max	0.12	0.62	0.008	0.012	0.48	9.14	0.18	0.94	0.14	0.022	0.02

Prior to examination, the specimen was mechanically polished using SiC abrasive papers and diamond paste followed by vibro-polishing with colloidal silica suspension to obtain a finely polished surface suitable for optical microscopy (OM), scanning electron microscopy in combination with energy dispersive X-ray spectroscopy (SEM-EDS) and laser Raman spectroscopy (LRS). The thickness of the oxide was measured at a fin tip.

A Carl Zeiss Sigma field emission gun scanning electron microscope (FEG-SEM) fitted with an Octane Plus™ EDS system from EDAX™ was used for SEM-EDS analysis. High resolution secondary electron (SE) images were obtained. TEAM EDS software was used for acquiring spectra and mapping. All the EDS analysis was undertaken at 15keV primary electron energy. The electron beam interaction volume for this analysis was estimated to be approximately 500 nm in diameter.

A Renishaw inVia Raman spectrometer incorporating a Leica optical microscope with a Leica N-plan 50x objective lens (NA=0.75) was used for acquisition of Raman spectra and maps. The instrument uses a 532 nm wavelength Nd: YAG laser. The maps and spectra were processed using Renishaw Wire version 4.3 software. The Raman map was obtained by scanning over a 40×40 µm region, moving the stage in 1 µm steps and acquiring for 40 s per point. 10% laser power was used to limit specimen damage, corresponding to 3mW power at the sample surface. Calibration was performed automatically using a silicon sample integral to the instrument.

Results

Optical micrographs of the metallurgically polished specimen and a region of oxide at the fin tip corner are shown in Figures 2 a) and b) respectively. The oxide thickness at this point was approximately 430 µm and the morphology of the oxide is multi-layered. A crack is present in the oxide, extending radially to the fin corner.

The thickness of the oxide, together with the presence of multi-layering and cracking is evidence that the specimen has entered the breakaway oxidation regime.

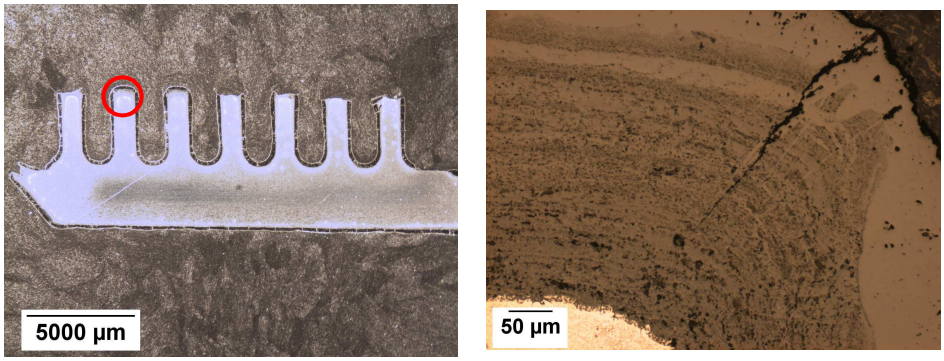

a) b)

Figure 2: Optical micrographs of the specimen a) low magnification b) a region close to the fin tip.

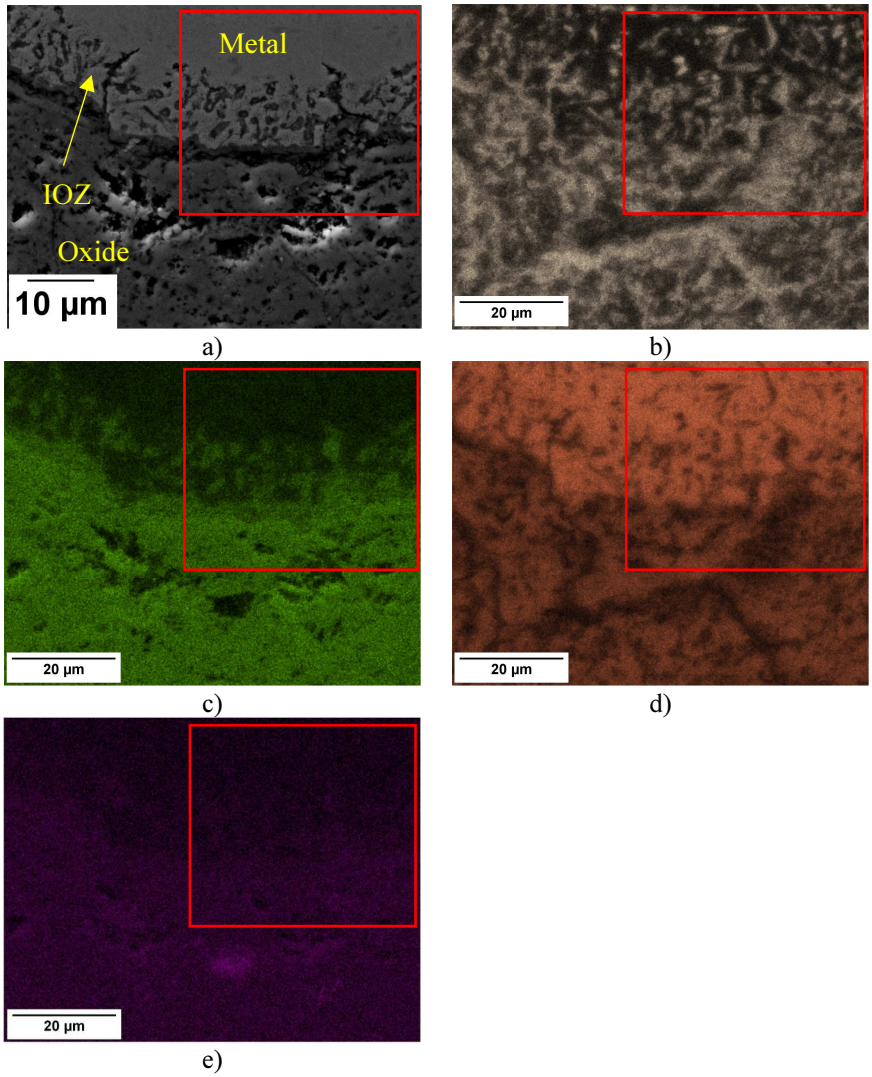

a) b) c) d) e)

Figure 3: a) Scanning electron micrograph. EDS maps of elements b) Cr; c) O; d) Fe and e) C. The marked area was mapped using scanning laser Raman spectroscopy.

Scanning electron micrographs and EDS composition maps of a region at the fin tip close to the metal/oxide interface are shown in Figure 3. Metal, internal oxidation zone (IOZ) and oxide regions are marked in the scanning electron image of Figure 3 a). Chromium is present as filamentary structures throughout the oxide and IOZ, and extends into the metal where it is associated with carbide precipitates. The iron map shows the opposite contrast and therefore composition distribution. The oxygen map shows the filamentary structures in the IOZ to

contain oxygen, while some depleted regions in the oxide layer are shown to contain carbon. The outlined regions in the images indicate an area that was mapped by scanning laser Raman spectroscopy.

A white light illuminated optical micrograph obtained from the Raman instrument is shown in Figure 4 a). The outline box shows the area mapped by Raman spectroscopy. Spectra obtained from two positions at A and B are shown in Figures 4 b) and 4 c) respectively. These are shown after baseline removal using an 11th order polynomial curve, and cosmic ray removal.

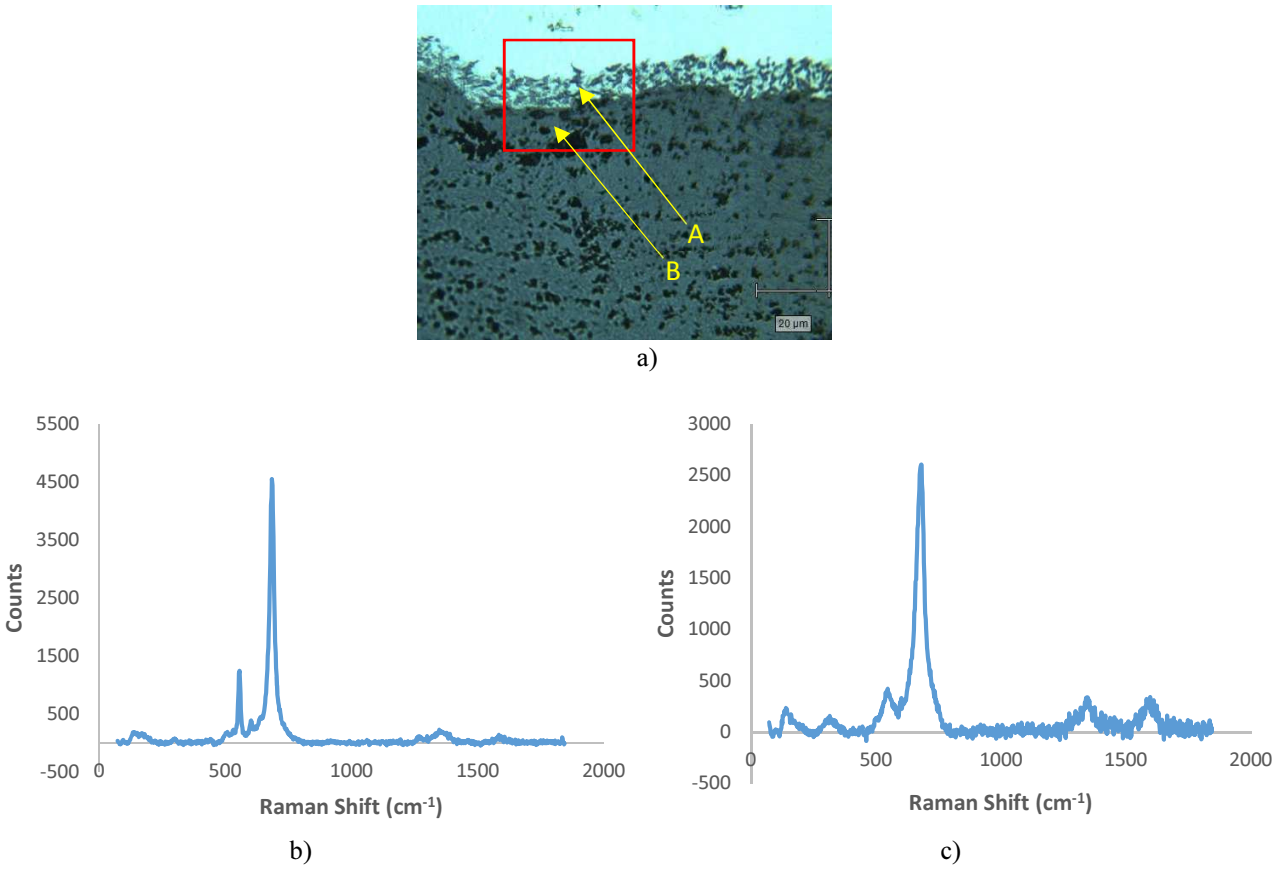

Figure 4 a) White light optical micrograph of specimen showing region mapped by Raman spectroscopy. b) Raman spectrum from point A. c) Raman spectrum from point B.

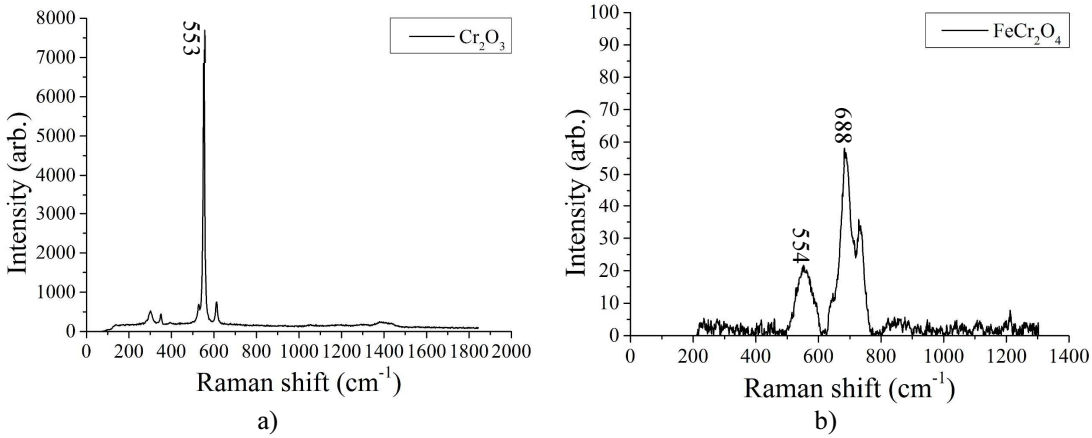

Figure 5: Raman spectra from a) Cr_2O_3 obtained here and b) $FeCr_2O_4$ from the RRUFF database[15].

For comparison, a Raman spectrum was obtained from a pure sample of chromium (III) oxide (chromia, Cr_2O_3) obtained from U.S. Department of Commerce. The spectrum is shown in Figure 5 a), while Figure 5 b)

shows a reference Raman spectrum obtained from the spinel chromite ($FeCr_2O_4$) taken from the Raman database RRUFF[15].

The Raman spectra for both Cr_2O_3 and $FeCr_2O_4$ contain peaks at around 553 cm^{-1}, but for the former the peak is much narrower, corresponding to the A_{1g} mode[13] and accompanied by a smaller peak at 610 cm^{-1}. For the $FeCr_2O_4$ reference spectrum, the peak at 554 cm^{-1} is broad, and there is a further peak at about 684 cm^{-1}. Both of these materials appear to be present within the complex oxide of the 9Cr-1Mo sample analysed here. The spectrum from position A in Figure 4 a) contains a narrow peak at 555 cm^{-1} accompanied by a smaller peak at 610 cm^{-1}, as shown in Figure 4 b), consistent with Cr_2O_3, while position B, Figure 4 c, shows a broad peak at 555 cm^{-1} with a further broad peak at 684 cm^{-1} consistent with $FeCr_2O_4$. It is also apparent that for many positions the Raman spectra are mixtures of the two types, presumably because of the limited spatial resolution of the technique.

Two further main peaks are present in the spectra from the oxide here; one at 1350 cm^{-1} and a second at 1587 cm^{-1} in Figures 4b) and c). These are consistent with spectra from carbon in the form of graphite with the low-degree order.

Raman intensity distribution maps of area marked in Figure 3 were obtained from the 555, 684 and 1350 cm^{-1} peaks by extracting local peak intensity values and plotting them as a function of position, shown in Figure 6.

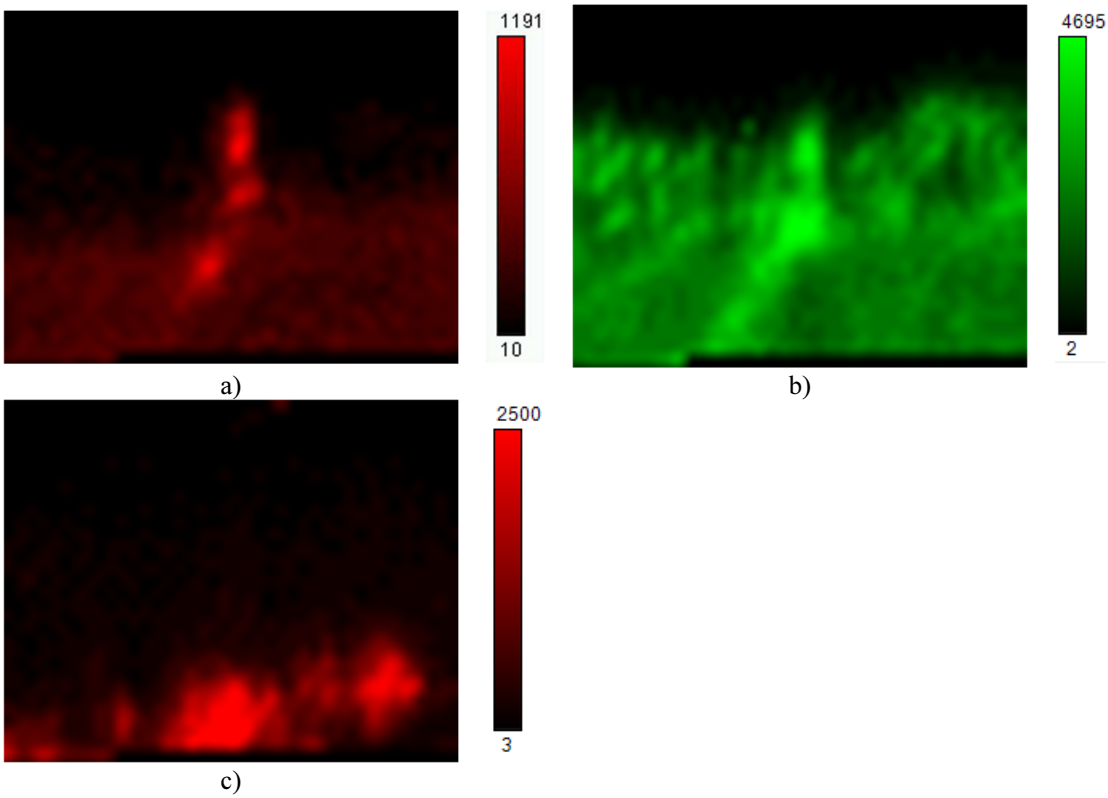

Figure 6. Raman peak intensity maps for peaks at a) 555 cm^{-1}, b) 684 cm^{-1} and c) 1350 cm^{-1}. The intensity scale markers in counts per pixel are shown for each map.

By observing the Raman spectra at each position in the maps, it can be demonstrated that the bright regions in the 555 cm^{-1} intensity map of Figure 6 a) correspond to the narrower peaks at 555 cm^{-1} and 600 cm^{-1} associated with Cr_2O_3 while the diffuse regions at the lower part of the image are consistent with the spectrum for chromite, $FeCr_2O_4$. The intensity map for the 684 cm^{-1} peak is shown in Figure 6 b) indicating the presence of chromite

in the majority of the oxide, extending into the filamentary structures of the IOZ. The bright regions in the lower part of the 1350 cm^{-1} map of Figure 6 c) indicate the presence of graphite with the low-degree order. It can be noted that while the peak intensity maps are consistent with the EDS element maps, but the Raman spectra reveals further information about the types of oxide present within the scale.

Discussion

The sample of 9Cr-1Mo steel examined here has entered breakaway oxidation, as shown by its thick multi-layered oxide at the fin tip and the presence of a crack aligned radially from the fin tip corner near the metal/oxide interface to the outer surface of the duplex layer. SEM and EDS data obtained close to the metal/oxide interface are consistent with those found previously in breakaway oxidised samples[16], indicating a spinel layer containing some deposited carbon, an IOZ layer with filamentary oxide structures and chromium-rich carbides within the metal. The scanning laser Raman spectroscopy has provided further information on types of oxide present, confirming the presence of the spinel chromite ($FeCr_2O_4$) and also chromia (Cr_2O_3) which appears distributed in small areas close to the IOZ layer. The technique also identified the graphite with the low-degree order presents in patches within the spinel[17].

The oxidised region evaluated in Figure 3 has a complex morphology, and while the onset of breakaway oxidation is clearly linked to sample geometry, it is not clear whether the cracking that often occurs within the oxide scale is the cause of breakaway by allowing ingress of gas to the metal-oxide interface, or whether breakaway is triggered by the high carbide content within the metal which gives rise to a rapidly moving oxidation front, with cracking occurring as a result of this rapid growth. Moreover, the process is potentially exacerbated by the multi-layering of spinel and magnetite. The complexity of the oxide system complicates the measurement of strain because any shift in the position of a specific Raman peak may be due to strain, a change in oxide type, the presence of an impurity element or a combination of these[18-20]. The position of the main Cr_2O_3 peak for the reference sample was 553 cm^{-1}, while that obtained from the chromia within the 9Cr-1Mo sample was at 555 cm^{-1}. This preliminary work would suggest a compressive stress of 0.5 MPa following the investigation and calibration undertaken by Birnie et al[14]. But this indicative stress assumes that there are no stresses within the reference sample and, more importantly, that there are no compositional effects present. The identification of some of the oxide types present within the material however, confirms the value of scanning laser Raman spectroscopy for investigating these complex oxidation processes that occur within the ferritic 9Cr-1Mo steel components.

Conclusion

Optical and scanning electron microscopy, energy dispersive X-ray analysis and Raman spectroscopy have been combined to analyse a region of 9Cr-1Mo steel in breakaway oxidation. Chromite ($FeCr_2O_4$), chromia (Cr_2O_3) and graphite with the low-degree order were identified by Raman spectroscopy and peak intensity maps were used to show their locations with a spatial resolution of approximately 1 μm. The complexity of the oxide structure present complicates the measurement of strain in the material.

Acknowledgements

Financial support from EDF Energy Ltd and China Scholarship Council is gratefully acknowledged. The views expressed are that of the authors and not of EDF Energy Ltd.

References

[1] E. Nonbel, Description of the Advanced Gas Cooled Type of Reactor (AGR), Risoe National Laboratory Roskilde, Denmark, (1996).

[2] M. G. Angell, S. K. Lister and A. Rudge, The effect of steam pressure on the oxidation behaviour of annealed 9Cr-1Mo boiler tubing material, 15th International Conference on the Properties of Water and Steam (ICPWS XV), Berlin, Germany, September 8-11 (2008)

[3] M. N. H. Comsan, Status of Nuclear Power Reactor Development, 6th Conference on Nuclear and Particle Physics, Luxor, Egypt, November 17-21 (2007).
[4] A. S. Khanna, P. Rodriguez and J. B. Gnanamoorthy, Oxidation Kinetics, Breakaway Oxidation, and Inversion Phenomenon in 9Cr-1Mo Steels, Oxidation of Metals, 26 (1986): 171-200
[5] R. A. Brierley and B J Handy, A Survey of the Oxidation Induced Carburisation of 9Cr-1Mo Steel in AGR Coolant Atmospheres, British Energy, 1 (2007): 13490/TR/001.
[6] A. M. Pritchard, N. E. W. Hartley, J. F. Singleton and A. E. Truswell, Oxygen-18 and Deuterium Profiling in Thick Films on Fe-9% Cr Alloys by 3 MeV Nuclear Microprobe, Corrosion Science, 20 (1980): 1-17
[7] L. Martinelli, C. Desgranges, F. Rouillard, K. Ginestar, M. Tabarant and K. Rousseau, Comparative oxidation behaviour of Fe-9Cr steel in CO_2 and H_2O at 550° C: Detailed analysis of the inner oxide layer, Corrosion Science, 100 (2015): 253-266
[8] G. B. Gibbs and R. Hales, the Influence of Metal Lattice Vacancies on the Oxidation of High Temperature Materials, Corrosion Science, 17 (1977): 487-507
[9] T. Gheno, D. Monceau, J.Q. Zhang and D.J. Young, Carburisation of Ferritic Fe-Cr alloys by low carbon activity gases, Corrosion Science, 53 (2011): 2767-2777
[10] H. O. Andren, G. J. Cai and L. E. Svensson, Microstructure of heat resistant chromium steel weld metals, Applied Surface Science, 87/88 (1995): 200-206
[11] F. Rouillard, G. Moine, M. Tabarant and J. C. Ruiz, Corrosion of 9Cr Steel in CO_2 at Intermediate Temperature II: Mechanism of Carburization, Oxidation of Metals, 77 (2012): 57-70
[12] M. Vijayalakshmi, S. Saroja, V. T. Paul, R. Mythili and V. S. Raghunathan, Microstructural Zones in the Primary Solidification Structure of Weldment of 9Cr-1Mo Steel, Metallurgical and Materials Transaction A, 30A (1999): 161-174
[13] X. Y. Zhong, X. Q. Wu and E. H. Han, The characteristic of oxide scales on T91 tube after long-term service in an ultra-supercritical coal power plant, The Journal of Supercritical Fluids, 72 (2012): 68-77
[14] J. Birnie, C. Craggs, D. J. Gardiner, and P. R. Graves, Ex Situ and in situ Determination of Stress Distributions in Chromium Oxide Films by Raman Microscopy, Corrosion Science, 33 (1992): 1-12
[15] James Shigley, Chromite R110059 [DB/OL], http://rruff.info/chem=Cr,O,Fe/display=default/R110059, (18th March, 2017)
[16] A. S. Khanna, P. Rodriguez, J. B. Gnanamoorthy, Oxidation Kinetics, Breakaway Oxidation, and Inversion Phenomenon in 9Cr-1Mo Steels, Oxidation of Metals, 26 (1986): 171–200
[17] A. C. Ferrari and J. Robertson, Interpretation of Raman spectra of disordered and amorphous carbon, Physical Review B, 61 (2000): 14095-14107
[18] K. F. McCarty and D. R. Boehme, A Raman Study of the Systems $Fe_{3-x}Cr_x0_4$ and $Fe_{2-x}Cr_x0_3$, Journal of Solid State Chemistry, 79 (1989): 19-27
[19] T. Gheno, D. Monceau and D.J. Young, Mechanism of Breakaway Oxidation of Fe–Cr and Fe–Cr–Ni Alloys in Dry and Wet Carbon Dioxide, Corrosion Science, 64 (2012): 222-233
[20] K. Natesan, Z. Zeng and D. L. Rink, Materials Performance of Structural Alloys in CO_2 and in CO_2-Steam Environments, Proceedings 22nd Annual Conference on Fossil Energy Materials, Pittsburgh, PA, June 8-10, 2008.